Boosting catalytic combustion of diesel soot particles over potassium-promoted CoMn-Co$_3$O$_4$ dual spinel structure catalyst

Runhan Niu, Congcong Li, Qilong Guo, Panpan Liu, Changsen Zhang [*]

School of Ecology and Environment, Zhengzhou University, Zhengzhou, Henan 450001, PR China

ARTICLE INFO

ABSTRACT

Catalytic oxidation is an effective method to remove soot particles from diesel exhaust, and the key aspect of this technology is to develop highly effective catalysts. In this work, a potassium-promoted dual spinel structure was prepared for soot elimination with the self-sacrificing template strategy. The highest activity was presented by the CoMn-0.2 H-10%K catalyst under a loose contact mode, with the temperature of soot conversion reaching 90% and turnover frequency value of 365 $^\circ$C and 3.76×10^{-3} s^{-1}, respectively. The catalyst was found to have a high content of oxygen vacancy and a superior ability for lattice oxygen migration, which led to elevated performance for soot combustion. The formation of K-OMS-2 at the interface between the CoMn spinel and the Co$_3$O$_4$ spinel was one of the reasons for the elevated lattice oxygen migration at low temperatures. This work provides an effective way to prepare transition metal catalysts for soot combustion.

1. Introduction

Soot particles in diesel exhaust have adverse impacts on both the environment and human well-being and are an important component of fine particles in air pollutants [1]. Currently, the diesel particle filter (DPF) is the most economical and effective after-treatment technology for regulating and reducing soot emissions [2]. Coating the DPF filter with a suitable catalyst (so-called CDPF) to achieve in-situ low-temperature combustion of soot can solve the problem of DPF clogging during vehicle operation [3]. Consequently, the production and application of after-treatment technology predominantly depend on the design and development of catalysts with low cost, remarkable activity, and outstanding stability.

Nowadays, the DPF coated catalyst of the diesel vehicle exhaust assembly is mainly based on precious metals as the essentially active components [4,5]. Considering the cost and large-scale application, previous research focuses on the substitution of precious metals, with transition metals (Co, Mn, etc.) and their oxides, which showed promise of the application for soot combustion [4,6–8]. Co$_3$O$_4$ spinel is well-known to be an effective transition metal oxide for the removal of soot and other pollutants (e.g. CO and hydrocarbons) from diesel vehicle exhaust. [9,10] Shen et al. [10] reported that adjusting the strength of the Co-O bond in Co$_3$O$_4$ can increase the content of active oxygen species on the catalyst surface. Cui et al. [11] confirmed that the high

activity is attributed to the abundant cationic vacancies and strong oxygen mobility of the nanoflower spinel CoMn$_2$O$_4$ during the toluene catalytic oxidation process. Manganese oxides have abundant valence and variable crystal structures [12,13]. Particularly, compared to other crystal structures, the octahedral layered structures (OL-1) and octahedral molecular sieves (OMS-2) have greater catalytic activity. Furthermore, potassium ions were typically doped into the aforementioned crystal structures because of their structural support and capacity to donate electrons, resulting in the formation of K-OMS-2 and K-OL-1 materials [14].

Strategies for improving catalyst activity include interface engineering [15,16], defect engineering [17] and morphology engineering [18,19]. Among them, interface engineering has received extensive attention due to its ability to enhance the interaction between different components. This interfacial interaction typically modulates the electronic structure, oxygen vacancy content, and lattice oxygen mobility of the composite catalyst. These properties of the catalyst are crucial for the soot combustion reaction [20]. It can be anticipated that using the spinel structure known for its stability and simultaneously enhancing the interfacial interaction between different spinel oxides may be effective in boosting soot combustion. Wang et al [21]. reported the interfacial interaction between CeO$_2$-based oxides and perovskite (LaMnO$_3$/LaFeO$_3$) for soot oxidation, indicating that the interfacial interaction can create more reactive oxygen species. Zhu et al [22].
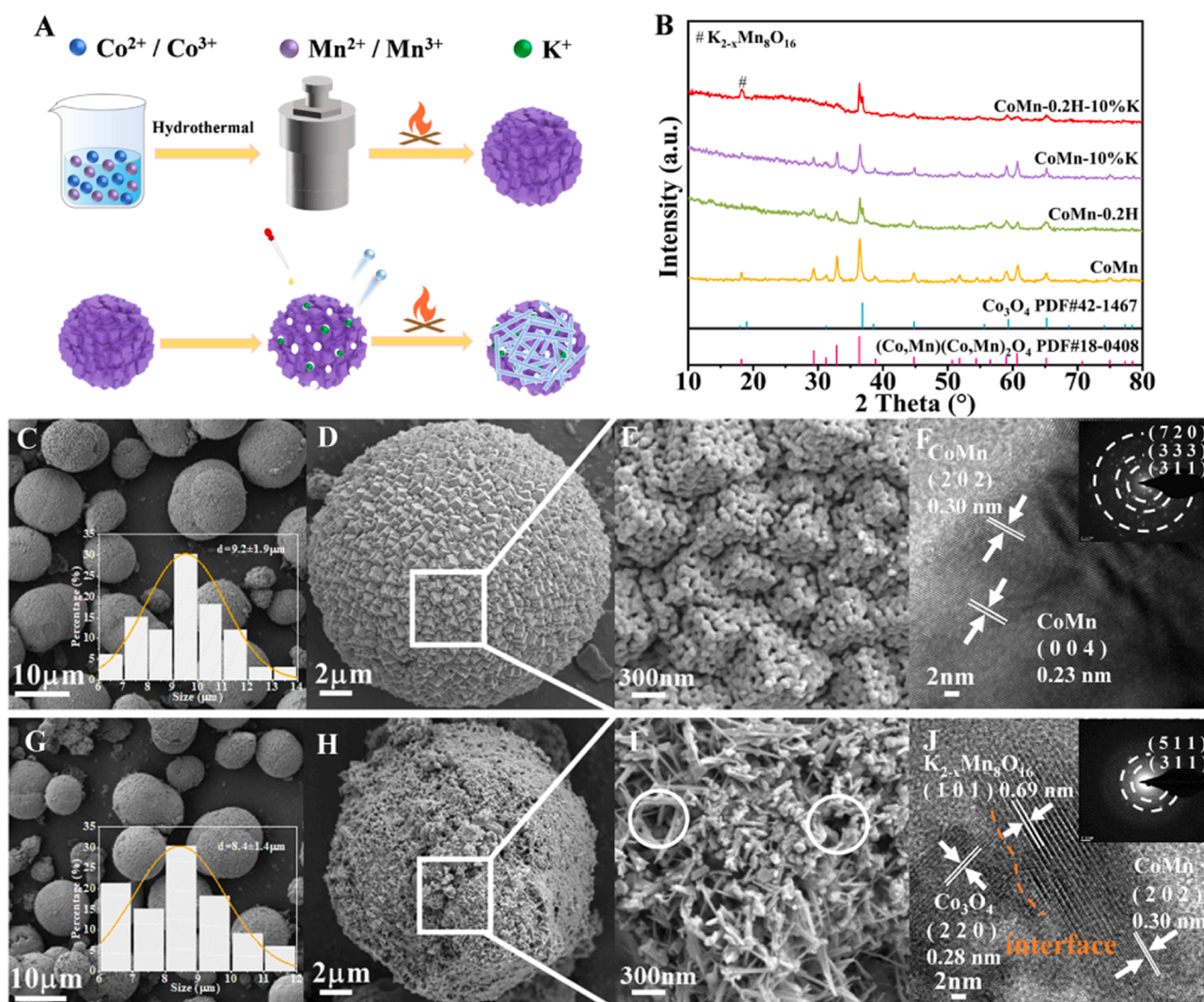
Fig. 1. (A) Schematic illustration of the synthesis procedure for CoMn and CoMn-0.2 H-10%K, (B) XRD patterns of CoMn, CoMn-0.2 H, CoMn-10%K and CoMn-0.2 H-10%K, (C-E) SEM and (F) TEM images of CoMn, (G-I) SEM and (J) TEM images of CoMn-0.2 H-10%K.

adopted a surfactant-assisted strategy to develop $CuO-Fe_3O_4$ bimetal oxides with enhanced interfacial effects for VOCs oxidation.

Herein, we prepared a potassium-promoted dual spinel structure catalyst with the self-sacrificing template strategy and used it for soot combustion. Physical-chemical properties of the catalyst were characterized and their effects on the soot combustion were investigated in detail. In addition, the oxygen vacancy and active oxygen within the prepared catalyst were examined. To illustrate the elevated performance of catalysts, density function theory (DFT) was performed to calculate the oxygen vacancy formation energy, oxygen adsorption energy and density of states. This work reveals that the dual spinel structure catalyst could be a promising catalyst for efficient soot combustion.

2. Experimental

2.1. Preparation of catalysts

In a typical technique, a clear solution was prepared by dissolving urea (40 mmol), Co $(NO_3)_2 \cdot 6$ H_2O (4 mmol), and Mn $(CH_3COO)_2 \cdot 4$ H_2O (8 mmol) in 60 mL of deionized water, followed by 10 minutes of agitation. Subsequently, the resulting mixture was transferred to a 100 mL stainless steel Teflon-lined autoclave and subjected to a 6-hour reaction at 120 °C. After filtering, the precipitate underwent three rounds of washing in ethanol and deionized water. Following that, 8 h of

drying at 60 °C, the powder of CoMn LDH (layered double hydroxide) with urchin structure was obtained [23]. Ultimately, CoMn spinel oxides were created by annealing CoMn LDH for one hour at 300 °C in the air, followed by two hours at 500 °C.

A mixed aqueous solution of KNO_3 (5–15 wt%) and 5 mL diluted HNO_3 (0.1–0.3 M) was added to 1 g of the aforementioned CoMn spinel oxide, and the mixture was agitated for five hours at room temperature. It was then dried for one hour at 120 °C, and finally calcined for 2 hours at 500 °C (Fig. 1A). The samples that were collected after acid etching and potassium support were designated as CoMn-xH-yK, where x and y stand for the HNO_3 aqueous concentration (M) and the potassium load (wt%), respectively. For comparison, CoMn spinel oxide that was treated by dilute 0.2 M HNO_3 (without KNO_3) was labeled as CoMn-0.2 H; and by KNO_3 (10 wt%) was denoted as CoMn-10%K.

2.2. Characterizations

Detailed characterization methods are described in the Supporting Information, including X-ray diffraction (XRD), scanning electron microscope (SEM) and energy dispersive spectroscopy (EDS), transmission electron microscope (TEM), high-angle annular dark-field (HAADF), X-ray Fluorescence (XRF), Fourier transform infrared (FT-IR) spectroscopy, N_2 adsorption-desorption, X-ray photoelectron spectroscopy (XPS), Electron paramagnetic resonance (EPR), H_2 temperature

programmed reduction (H$_2$-TPR), O$_2$ temperature programmed desorption (O$_2$-TPD), soot temperature programmed reduction (Soot-TPR) and NH$_3$ temperature programmed desorption (NH$_3$-TPD).

2.3. Activity Measurements

The catalyst and soot are mixed in a fixed ratio of 10:1 in different contact modes. The temperature-programmed oxidation of soot (Soot-TPO) experiments were performed under various atmospheres using the reaction setup shown in Scheme 1 of the Supporting Information to evaluate the activity of the prepared catalysts.

The catalytic activity was assessed through the determination of T$_{10}$, T$_{50}$, and T$_{90}$, representing the temperatures corresponding to 10%, 50%, and 90% of soot conversions, respectively. The soot conversion rate (X %) is computed according to the formula:

$$X\% = \frac{[CO]_t + [CO_2]_t}{[CO]_T + [CO_2]_T} \times 100\%$$

Here, $[CO]_T + [CO_2]_T$ represents the total amount of CO and CO$_2$ generated, while $[CO]_t + [CO_2]_t$ signifies the combined amount of CO and CO$_2$ generated before reaching a certain temperature.

The selectivity towards CO$_2$ (S_{CO_2}) is defined as the ratio of CO$_2$ outlet concentration (C_{CO_2}) to the sum of CO$_2$ and CO outlet concentrations, as expressed by:

$$S_{CO_2} = \frac{C_{CO_2}}{C_{CO} + C_{CO_2}}$$

In this equation, C_{CO_2} and C_{CO} represent the concentrations of each carbon species produced during soot oxidation.

The apparent activation energy (Ea) and turnover frequency (TOF$_{ov}$) were calculated according to the method reported in the literature [24], and detailed explanations were given in the Supporting Information.

2.4. DFT calculations

All the spin-polarized density functional theory calculations corrected by on-site Coulomb interaction (DFT+U) were conducted by first-principles calculations. Calculations were performed with a plane-wave energy cutoff of 400 eV and a k-point mesh of 4×1×1 using the Monkhorst-Pack scheme. The Ueff of Mn and Co in this study was set to 3.0 eV and 4 eV [25]. The vacuum layer was set to be 15 Å above the surface. In the calculation process, the lower two atomic layers were fixed. Energy convergence was set to 10^{-5} eV, and force convergence was set to 0.01 eV·Å^{-1} for electronic structure calculations. Other information and specific formulas for DFT calculations are summarized in the Supporting Information.

3. Results and discussion

3.1. Characterizations of the catalysts

The XRD images of the catalysts prepared with different acid concentrations and potassium loadings are shown in Fig. 1B and Fig. S1. Fig. 1B illustrates the XRD pattern of the CoMn spinel, establishing its conformance with the crystalline structure of (Co, Mn) (Co, Mn)$_2$O$_4$ (PDF#18–0408) [26]. No new peak was observed after loading potassium (CoMn-10%K), and the crystallinity decreased, reflecting that the potassium species may be amorphous. The spinel structure can be partially retained by the acid-etched catalysts (CoMn-0.2 H, CoMn-0.2 H-10%K), but they can also create new phases. A characteristic peak of Co$_3$O$_4$ (PDF#42–1476) appears at 36.8°, indicating selective dissolution of Co. Interestingly, the characteristic peak of K$_{2-x}$Mn$_8$O$_{16}$ (K-OMS-2) (PDF#44–1386) was observed at 18.3° after the acid treatment and potassium loading. This result indicated the formation of K-OMS-2 in the catalyst during the preparation [13]. The

Table 1
Textural property of catalysts.

Catalysts	Crystallite size[a] (nm)	S$_{BET}$[b] (m^2 g^{-1})	Total pore volume[c] (cm^3 g^{-1})	Pore size[c] (nm)
CoMn	12.07	2.59	0.015	7.48
CoMn-0.2 H	9.85	22.61	0.073	11.18
CoMn-10%K	12.51	0.68	0.005	9.15
CoMn-0.2 H-10%K	12.26	16.74	0.031	15.89

[a] Calculated using the Scherrer equation based on the diffraction peak in XRD.
[b] Calculation from the BET method.
[c] Obtained by the BJH method.

formation of K-OMS-2 was proposed as follows: Mn^{3+}, which is extremely susceptible to the disproportionation-precipitation reaction, was exposed to an acidic solution when the Co atom was removed. This resulted in the conversion of Mn^{3+} into Mn^{2+} and Mn^{4+}, as per the overall reaction: 2Mn^{3+}→Mn^{4+} + Mn^{2+}, then K$^+$ combines with Mn^{4+} to form K-OMS-2 [27]. The introduction of K$^+$ in the catalyst could balance charge among various manganese species (Mn^{2+}, Mn^{3+}) in the 2×2 tunnel structure composed of [MnO$_6$]. In addition, the formation of K-O bonds facilitated structural stability [28].

In order to delve deeper into the effects of acid etching and potassium support on the structure and activity of the catalysts, specific characterization data was examined for CoMn, CoMn-0.2 H, CoMn-10%K and CoMn-0.2 H-10%K. The Scherrer formula was used to compute the particle size of the catalyst (Table 1), and the outcomes showed that acid etching and potassium loading minimally affected the crystal phase and size of the catalyst. Compared with CoMn spinel, the grain size of CoMn-0.2 H decreased, indicating that nitric acid can etch the surface of CoMn spinel. According to the grain size of CoMn-10%K and CoMn-0.2 H-10% K catalysts, it can be seen that the loading of K did not affect the crystal phase and size of the support. The results of CoMn-0.2 H and CoMn show that acid etching can increase the specific surface area of the catalyst. Nevertheless, after the introduction of K (CoMn-0.2 H-10%K), the value decreased to 16.4 m^2·g^{-1}. This result may be due to the partial coverage of the catalyst by the K species. Besides, the findings of the N$_2$ adsorption-desorption tests on the four catalysts (Table 1 and Fig. S2) indicated the specific surface area of CoMn-0.2 H-10%K is larger than that for CoMn.

SEM images were used to depict the shape of the catalysts, as seen in Fig. 1 and S3. Fig. S4 shown the elemental mapping results of the prepared catalystsThe images demonstrated CoMn (Fig. 1C) with an average diameter of 9.2±1.9 μm, and CoMn-0.2 H-10%K (Fig. 1G) with an average diameter of 8.4±1.4 μm. Each 3D hierarchical cube-stacked microsphere in the CoMn spinel sample is made up of aggregated cubes (Figs. 1D-E). The surface of CoMn-10%K is smoother than CoMn (Fig. S3), possibly due to the coating of amorphous potassium species, which is consistent with XRD results. After acid etching (CoMn-0.2 H), part of the surface became rough, and some rod-like structures were observed coating the surface of the catalyst (Fig. S3). Fig. 1I displays the micrograph of CoMn-0.2 H-10%K, revealing rod-like structures on its surface. Notably, the surface gaps measure approximately 300±10 nm, surpassing the size of soot particles, and thus, facilitating enhanced gas exchange during the catalytic reaction. To determine the composition of the rod-like structure, we identified the lattice fringe spacings in TEM images (Figs. 1 and S5). The CoMn spinel phases (d (2 0 2) = 0.30 nm) and the lattice fringe spacing of 0.28 and 0.69 nm for CoMn-0.2 H-10%K (Fig. 1J) could both correspond well with the (2 2 0) plane of Co$_3$O$_4$ and the (101) plane of K-OMS-2, demonstrating that the new phase was also formed and that the spinel structure of the treated sample remained intact. Apart from this, the lattice distortion and local blurring at the interface between K-OMS-2 and Co$_3$O$_4$ spinel were revealed from the image of the TEM (as marked by orange lines in Figs. 1G and S6) [22, 29]. To substantiate the presence of the dual spinel structure in the
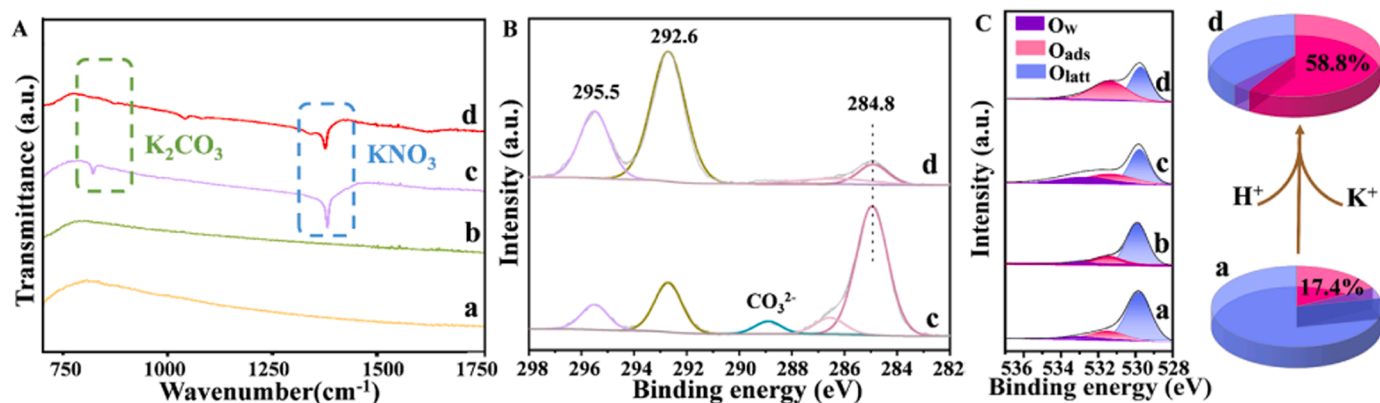
Fig. 2. (A) FT-IR spectra, (B) XPS spectra of C 1 s and K 2p, and (C) O 1 s ((a) CoMn, (b) CoMn-0.2 H, (c) CoMn-10%K, (d) CoMn-0.2 H-10%K).

catalyst, we present the HAADF, EDS and line scan results of CoMn-0.2 H-10%K (Figs. S7-S8). As associated with the results of the TEM, it is apparent that the outer rod-like substance is made of Co_3O_4, as Co and K elements are equally distributed across the image, while Mn elements exist only in the center of the image. The illustration in Figs. 1F and J shows that the crystal plane measured by the diffraction ring spacing corresponds well to the TEM results.

In addition to the crystal face of spinel, the image of CoMn-10%K (Fig. S5) reveals the presence of amorphous materials on the surface of the catalyst, potentially associated with the "free" K overlayer [30,31]. Potassium exists in two forms in the catalyst [32]: "stable" K species, which enter the lattice or interact strongly with atoms on the surface or subsurface, can enhance the intrinsic activity of the catalyst for soot oxidation [33]; carbonates and nitrates ("free" K species) with low melting points and great mobility, can improve the efficiency of catalyst-soot interaction [34]. However, excessive "free" potassium will cover the active surface of the catalyst or block the pores, resulting in the

inhibition of the reaction [32]. Although potassium-containing catalysts are one of the research hotspots [35], overcoming potassium loss is still a key challenge. The deactivation of such catalysts is mostly caused by the loss of the K element, which is the cause of this occurrence, whether they are loaded or doped with K [13]. It is crucial to find an effective strategy to promote the transformation of "free" K to "stable" K to accomplish successful anchoring of potassium and prevent the loss of potassium.

The catalysts were assessed using FT-IR and XPS to further establish the change in the form of potassium species (Fig. 2 and Fig. S9-10). The surface nitrate species induced by the undecomposed nitrate salts during the production of the catalyst were identified as the source of the FT-IR peaks at $1384\ cm^{-1}$ (blue box) on CoMn-10%K. [36] For the CoMn-0.2 H-10%K catalyst, the nitrate peak is still present, but the intensity is significantly reduced due to the residual nitrate caused by the incomplete decomposition of KNO_3. The surface carbonate potassium was also linked to a peak at $825\ cm^{-1}$ (green box) on CoMn-10%K, which was absent in CoMn-0.2 H-10%K (Fig. 2A) [37].
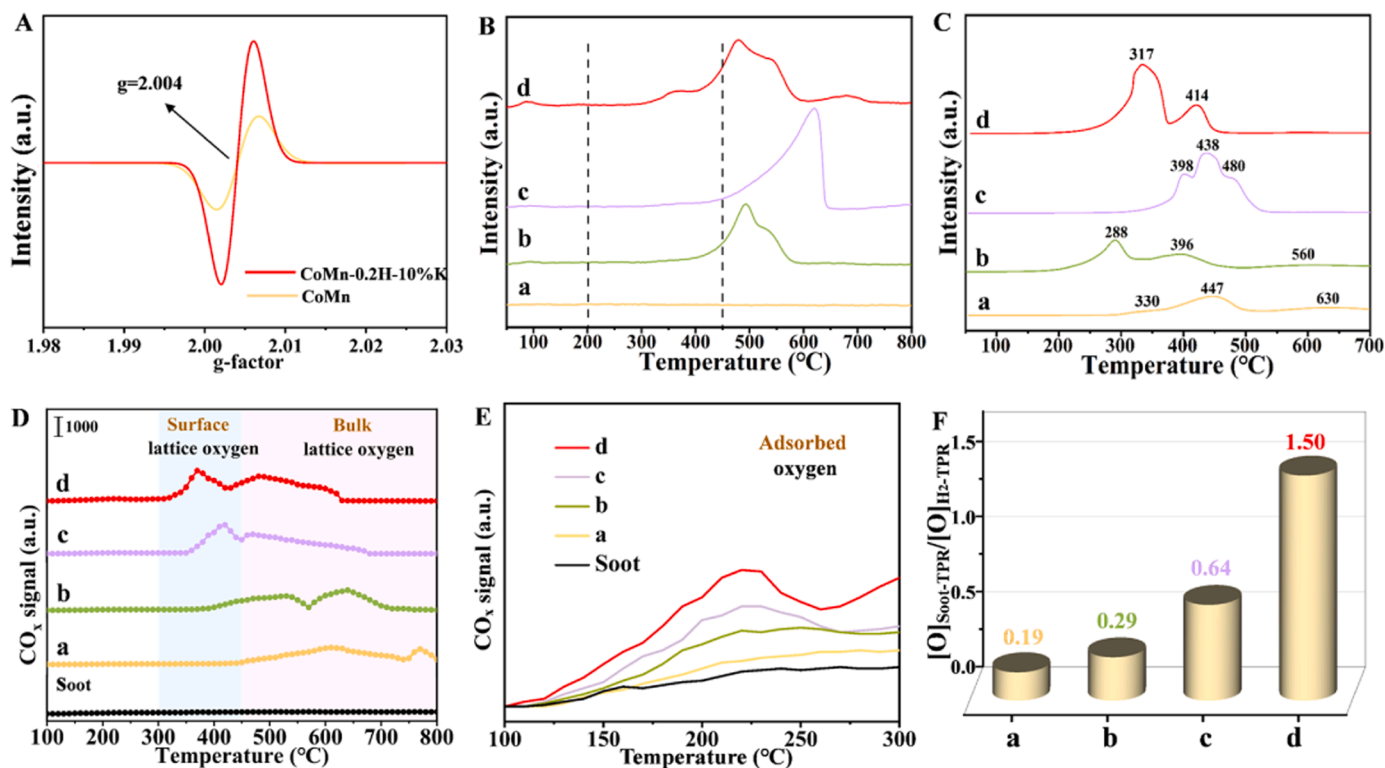

Fig. 3. (A) EPR spectra of the CoMn-0.2 H-10%K and CoMn, (B)O_2-TPD, (C) H_2-TPR (D) Soot-TPR comprehensive temperature range and (E) the temperature range of 100–300 °C, and (F) contact efficiency ((a) CoMn, (b) CoMn-0.2 H, (c) CoMn-10%K, (d) CoMn-0.2 H-10%K).
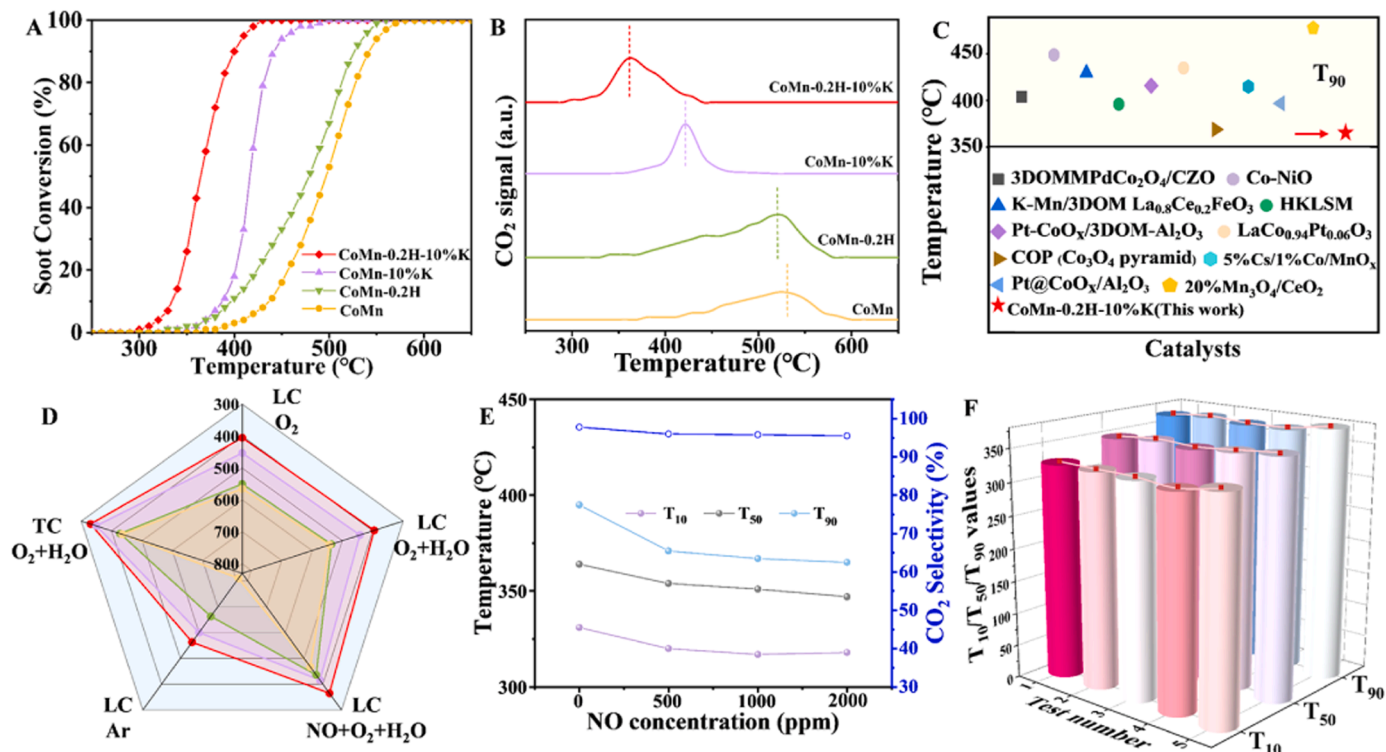
Fig. 4. (A) Soot conversion and (B) CO_2 concentration of as-prepared catalysts during Soot-TPO under loose contact conditions, (C) comparison for T_{90} value of CoMn-0.2 H-10%K and reported catalysts, (D) the catalytic performance under different contact modes and atmospheres (LC: loose contact; TC: tight contact), (E) the catalytic performance under different NO concentrations, (F) the stability of CoMn-0.2 H-10%K under loose contact.

The presence form of potassium species was subsequently confirmed through XPS analysis (Table S1). In Fig. 2B, XPS spectra of the C 1 s/K 2p region for CoMn-10%K and CoMn-0.2 H-10%K are presented. Within the C 1 s area of XPS, the presence of peaks in the range 287–290 eV are related to the carbonate species [38] and the N 1 s region is derived from NO_3^-. Compared with CoMn-10%K, the content of nitrate in CoMn-0.2 H-10%K was less, and there were no carbonate species. This result indicated a portion of "free" K combined with Mn to form the "stable" K (K-OMS-2), which agreed with the result of FT-IR. The Co^{3+}/Co^{2+} and Mn^{4+}/Mn^{3+} atomic ratios in CoMn-0.2 H-10%K surpassed those in CoMn, indicating that there was a reduced presence of Co^{2+} and an increased presence of Mn^{4+} exposed on the surface (Fig. S10 and Table S1). The higher average cation valence, along with the reduced (Mn + Co)/O ratio, suggests the generation of cation vacancies to maintain charge balance in CoMn-0.2 H-10%K (Table S1). As previously reported, Schottky defects within the spinel concomitantly induce oxygen and cation vacancies. [11] Oxygen-related oxidation processes are intricately linked to adsorbed oxygen and are notably influenced by oxygen vacancies. [39]

The O 1 s XPS spectra of the various catalysts were shown in Fig. 2 C. The surface binding energy of oxygen species dropped somewhat on the CoMn-10%K and CoMn-0.2 H-10%K catalysts, which may have been caused by the positive charge introduced by the dopant K^+ [40]. Three types of oxygen species may be distinguished from one another on the catalyst surface based on the area of split fitting and peak position (Table S1). Within the O 1 s spectra, we observe peaks at binding energies of 528.8, 531.1, and 533.6 eV, which can be attributed to lattice oxygen (O_{latt}), adsorbed oxygen related to surface oxygen vacancies (O_{ads}) and hydroxyl oxygen (O_W), respectively [22,41,42]. The amount of adsorbed oxygen (O_{ads}) was an important factors in catalytic soot oxidation [8]. Among these catalysts, CoMn-0.2 H-10%K showed the highest O_{ads} content of 58.8%, exceeding that of the original CoMn catalyst of 17.4% (Fig. 2C). EPR tests were used to measure the oxygen vacancy content on the surface of the catalyst (Fig. 3A). The high

intensity of the peak at g=2.004 in the EPR spectrum (Fig. S6) indicated that abundant oxygen vacancies were formed in CoMn-0.2 H-10%K [10, 12]. This result was consistent with the finding of XPS, which revealed the high oxygen vacancy content on the surface of the catalyst.

O_2-TPD experiments were conducted to delve deeper into the capabilities of oxygen adsorption and activation and the findings are displayed in Fig. 3B. The first peak observed on CoMn-0.2 H-10%K and CoMn-0.2 H before 200 °C corresponds to the physically adsorbed oxygen species, which may be a result of its porous structure and increased specific surface area [43]. The chemisorbed surface-active oxygen species correspond to the desorption peak in the range of 200–450 °C [6,8, 44]. For CoMn-0.2 H-10%K, the high intensity of desorption peaks of chemisorbed oxygen species were observed, which indicated the superior performance for soot combustation [45]. The lower the temperature of the desorption peak, the higher the mobility of lattice oxygen. The desorption peak temperatures of CoMn-0.2 H and CoMn-0.2 H-10%K are lower, indicating that the dual spinel structure can substantially enhance the migration ability of lattice oxygen. The desorption peak above 500 °C is caused by the desorption of the lattice oxygen of the catalyst [43,44]. Table S2 provides the O_2 desorption content for the 200–450 °C temperature range. Remarkably, CoMn-0.2 H-10%K exhibits the highest content, indicating its superior capacity for oxygen adsorption and storage, consistent with the results of XPS. At about 620 °C, a substantial peak was notably evident in the CoMn-10%K. This might due to the subsection decomposition of KNO_3: $KNO_3 \rightarrow KNO_2 + O_2$; $KNO_2 \rightarrow K_2O + O_2$ [36]. While the evident peak cannot be found in the CoMn-0.2 H-10%K, conclusively suggesting that nearly all the potassium nitrate participated in the formation of K-OMS-2 [46].

H_2-TPR was used to determine the redox capacities of the catalysts, as illustrated in Fig. 3 C. Based on the existing literature, MnO remains in a stable terminal phase when subjected to the H_2-TPR conditions employed in this study [47]. The reduction peaks found in the low-temperature region primarily correspond to the valence changes of various cations [7,12]. The reduction peak in high-temperature region is

attributed to the reduction of $Co^{2+} \rightarrow Co^0$ [12,48]. The CoMn catalyst exhibits broader and less intense peaks in comparison to other catalysts, signifying the enhanced capacity of the treated samples (CoMn-xH-yK) to facilitate more vigorous soot oxidation. The reductive peaks for CoMn at around 330 and 447 °C can be ascribed to the reduction of $Mn^{4+} \rightarrow Mn^{3+}$, $Mn^{3+} \rightarrow Mn^{2+}$ combined with $Co^{3+} \rightarrow Co^{2+}$, respectively [7,49]. The reduction reaction on the CoMn-0.2 H-10%K catalyst is marked by two distinct peaks: the first peak located at approximately 317 °C was assigned to the reduction of surface $Co^{3+} \rightarrow Co^{2+}$ combined with $Mn^{4+} \rightarrow Mn^{3+}$ while the second peak located around 414 °C was attributed to the reduction of $Mn^{3+} \rightarrow Mn^{2+}$ combined with bulk $Co^{3+} \rightarrow Co^{2+}$. Higher lattice oxygen mobility was said to be associated with higher hydrogen consumption, rendering it advantageous for soot combustion, and Table S2 displays the hydrogen consumption of the produced catalysts, with CoMn-0.2 H-10%K having the highest consumption. Interestingly, the $Co^{2+} \rightarrow Co^0$ reduction peak was not observed in CoMn-0.2 H-10%K, indicating that the deep reduction of the bulk phase of the composite was hindered, potentially enhancing the catalyst's operational durability [21].

Reactive oxygen species within catalyst could promote the soot combustion. The Soot-TPR experiments were performed under anoxic conditions, in which no extra oxygen was introduced into the system. The observed CO_2 production was then produced from the combination of soot and active oxygen species within the catalyst. Consequently, the result from the Soot-TPR could indicate the amount of active oxygen within the catalyst [50,51]. During Soot-TPR tests (anoxic), various lattice oxygen in the catalyst can migrate to the surface to participate in the reaction at high temperature. Then the deconvolution could be used to quantify the amount of active oxygen within the catalyst [37]. Fig. 3E also shows Soot-TPR results in the temperature range of 100–300 °C to further investigate desorbed oxygen species. The highest amount of CO_x was found for CoMn-0.2 H-10%K, suggesting an abundance of surface-adsorbed oxygen in the catalyst [6,7]. At the same time, the catalyst has a lower temperature peak in the range of 300 ~ 800 °C. These results suggest that the CoMn-0.2 H-10%K catalyst has a high lattice oxygen migration rate, which is consistent with the results of O_2-TPD [48]. The effective contact between the catalyst and soot particles constitutes a critical factor for interpreting catalytic performance. Given the facile permeation of H_2 molecules through most of the active sites on the catalysts, an evaluation of the total amount of reactive oxygen species across the catalysts can be achieved through H_2-TPR tests, denoted as $[O]_{H_2-TPR}$. Furthermore, the availability of catalyst surface/lattice oxygen accessible to soot can be determined by monitoring oxygen consumption (and CO_x production) in Soot-TPR tests, labelled as $[O]_{Soot-TPR}$. Subsequently, the accessibility of soot to the catalysts, proportional to the oxygen accessible to soot on the catalysts [52], can be quantified and normalized using the ratio of $[O]_{Soot-TPR}$ to $[O]_{H_2-TPR}$ [50, 53]. As shown in Fig. 3F and Table S2, the CoMn-0.2 H-10%K catalyst was with the highest ratio of $[O]_{Soot-TPR}/[O]_{H_2-TPR}$ (1.5), which implied the superior feasible of active oxygen by soot for the catalyst. In addition, the result of calculated the degree of relative contact (DRC) showed the close contact between the soot and the catalyst (Table S2).

3.2. Catalytic activities of prepared catalysts

The performances of as-prepared catalysts for soot combustion were assessed by the Soot-TPO method under LC spontaneously with the help of gas flow (Figs. 4A-B, Figure S11 and Table S3). The T_{90} of soot particulates in the absence of any catalysts reached a high of 621 °C, signifying a notably sluggish kinetics of soot oxidation without catalysts. In contrast to pure soot oxidation, it is evident that all samples exhibit a notable catalytic influence on soot combustion. The ranking of catalytic activities is as follows: CoMn-0.2 H-10%K > CoMn-10%K > CoMn-0.2 H > CoMn. It should be noted that the T_{90} value of the CoMn-0.2 H-10% K catalyst prepared in this study is 365 °C, which is comparable to

Table 2
Catalytic performance of reported catalysts under loose contact.

Catalyst	Soot/catalyst weight ratio	Reaction conditions	Heating rate	T_{90} (°C)	Ref
CoMn-0.2 H-10% K	1/10	2000 ppmNO + 5% O_2	5 °C/min	365	This work
Co-NiO	1/10	2000 ppmNO + 5% O_2	2 °C/min	449	[54]
3DOMMPdCo$_2$O$_4$/CZO	1/10	2000 ppmNO + 5% O_2	2 °C/min	404	[55]
HKLSM	1/9	500 ppm NO + 5% O_2	5 °C/min	396	[36]
LaCo$_{0.94}$Pt$_{0.06}$O$_3$	1/10	2000 ppmNO /air	10 °C/min	435	[5]
Pt-CoOx/3DOM-Al$_2$O$_3$	1/10	2000 ppmNO +5%O_2	2 °C/min	416	[56]
K–Mn/3DOM La$_{0.8}$Ce$_{0.2}$FeO$_3$	1/9	500 ppmNO +5%O_2	2 °C/min	430	[57]
COP (Co$_3$O$_4$ pyramid)	1/9	2000 ppmNO +5%O_2	2 °C/min	369	[58]
5%Cs/1%Co/MnOx	1/10	1000 ppmNO +10%O_2	2 °C/min	415	[8]
Pt@CoOx/Al$_2$O$_3$	1/10	2000 ppmNO +5%O_2	2 °C/min	397	[59]
20Mn$_3$O$_4$/CeO$_2$	1/9	50%air	2 °C/min	478	[60]

supported precious metal catalysts (Fig. 4C, Table 2 and Table S4). Fig. 4D summarizes the evaluation of the catalysts for soot combustion ability under different reaction conditions, the T_{90} of CoMn-0.2 H-10%K is the lowest, which is 330 °C in the tight contact mode.

In an actual diesel system, the catalyst is generally in loose contact with soot, and the effects of NO_x, SO_2 and water vapor cannot be ignored. [45] It has been reported that NO and water vapor play a positive role in the oxidation of soot, which is consistent with our experimental results (Fig. 4D and Table S3) [61]. NO will be oxidized to NO_2 in O_2, which is a stronger oxidizing agent than O_2, helps to accelerate the oxidation of soot [62]. The introduction of water could lead to the formation of *OH, which has a high oxide capacity [63]. In addition, the migration ability of *OH was higher than that of O_2, thus accelerating the regeneration rate of oxygen vacancies [63]. To examine the impact of NO, we conducted catalytic tests on the CoMn-0.2 H-10%K catalyst under varying NO concentrations (Fig. 4E and Table S5). In the absence of NO, the T_{90} value equated to 395 °C. However, the introduction of NO, even at the level of 500 ppm, noticeably enhanced the catalytic performance of the CoMn-0.2 H-10%K catalyst. With increasing NO concentrations, the catalytic activity exhibited only marginal improvement, and it had a negligible effect on CO_2 selectivity, which remained above 95% across all NO concentrations. These results underscore the significance of NO as a critical reactant in augmenting the catalytic activity of CoMn-0.2 H-10%K catalyst, albeit with limited incremental impact. To evaluate the sulfur resistance of the synthesized material in more detail, the catalytic activites of the CoMn-0.2 H-10%K catalyst were also examined under the presence of different SO_2 concentrations and water vapor conditions and the presence of NO, SO_2 and water vapor (Fig. S12A and Table S5). In the presence of water vapor, water molecules react with SO_2 to form sulfuric acid/sulfite, which can promote contact between soot particles and the catalyst by wetting the surface of the catalyst, thereby promoting the soot oxidation reaction. [6] It can be seen from Table S5 that the values of T_{10} and T_{50} increased after the introduction of SO_2. This result suggested that the activity of the catalyst decreased at low temperature. This may be due to the fact that the adsorbed SO_2 reacts with surface hydroxyl groups and reactive oxygen species to form sulfate/hydrogen sulfate salts, covering the surface active sites, thereby inhibiting soot combustion at low temperatures [64]. However, as the reaction temperature increases, the bisulfate species decomposes, and this inhibition is alleviated [56]. The result of NH_3-TPD (Fig. S13) revealed that the CoMn-0.2 H-10%K catalyst had a strong surface acidity, which could impede the adsorption of SO_2 and
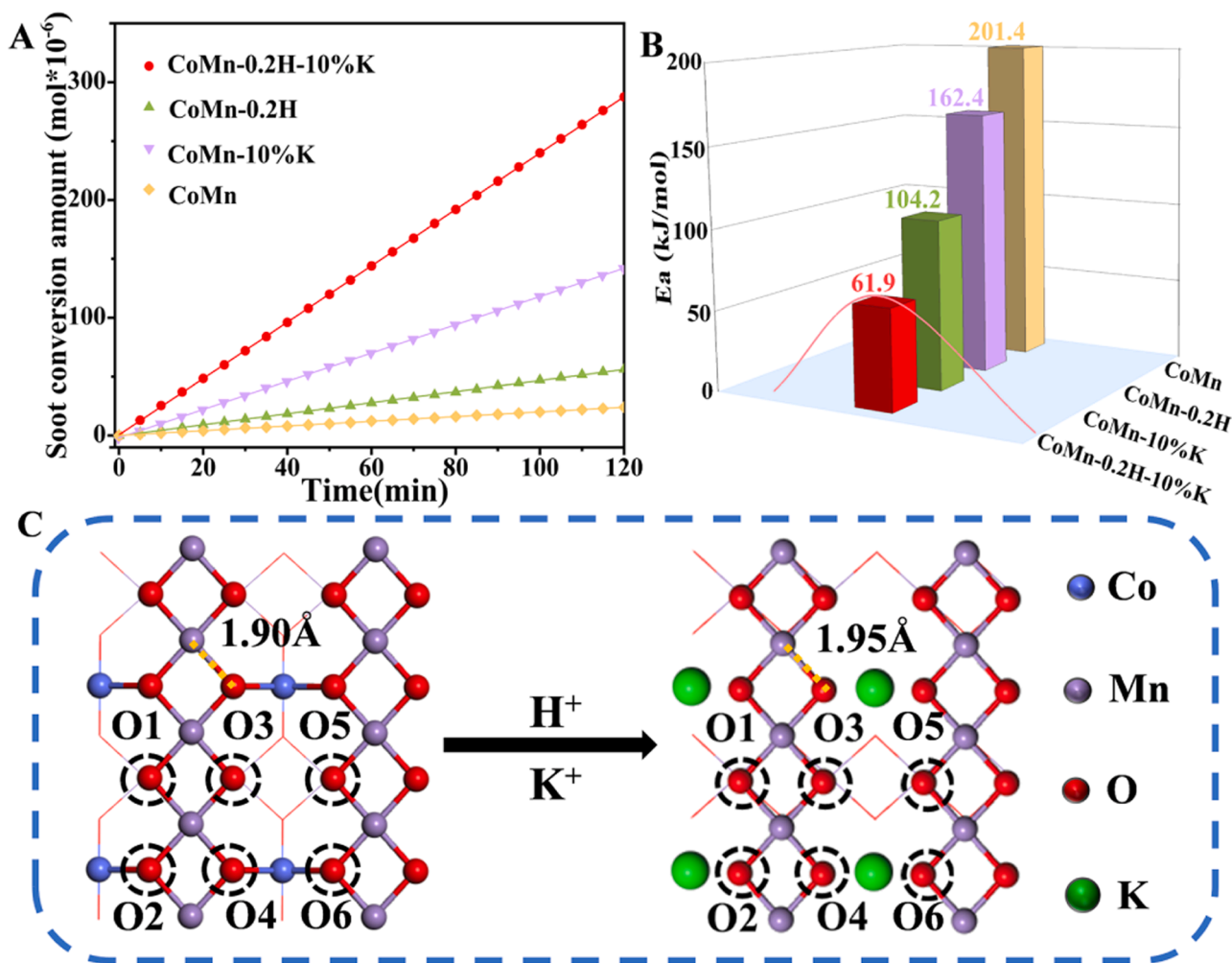
Fig. 5. (A) Soot conversion amounts as a function of time at 300 °C, (B) the *Ea* of as-prepared catalysts, (C) O atom position distribution in Bader charge analysis.

promote the decomposition of surface bisulfate. As a result, the resistance of SO_2 to the catalyst improved [56].

When designing catalysts for actual uses in the future, operational durability is a crucial consideration in addition to the impact of NO_x, SO_2 and water vapor. To imitate actual soot combustion conditions, the catalytic properties of CoMn-0.2 H-10%K and CoMn-10%K were tested in LC with NO and water vapor. The CoMn-0.2 H-10%K demonstrates excellent stability, maintaining consistent performance over 5 cycles, it was observed that variations of the T_{90} value equal to 370 ± 5 °C (Fig. 4F and Table S6) and the CO_2 selectivity were all higher than 95%. Unexpectedly, the CoMn-10%K with similar superior performance dramatically increased the temperature of T_{90} from the original 442–545 °C after repeated use for 5 times (Fig. S12B). It is critical to understand why the catalyst deactivates in order to develop superior activity catalysts, so we used XRF characterization to analyze CoMn-0.2 H-10%K and CoMn-10%K before and after cycles (Table S6). After the reaction, the K content of CoMn-0.2 H-10%K decreased by 6%, and the K content of CoMn-10%K decreased by 67%. In addition, the catalyst was washed with water for 24 h and the change of K content before and after washing was detected (Fig. S12C and Table S6). It can be further verified that K is confined in the channel after the simultaneous processing of etching and load. This strategy realizes the efficient anchoring of K and prevents its loss.

TOF_{ov} is defined as the ratio of the reaction rate (R) to the amount of active sites. Since the specific active sites cannot be measured, we used the number of reactive oxygen species to roughly evaluate them. And the amounts of active sites on the catalysts are obtained by isothermal

Table 3
Intrinsic activity parameters of as-prepared catalysts.

Catalysts	R (mol·s^{-1} g^{-1}×10^{-7})	O* (mol·g^{-1}×10^{-7})	TOF_{ov} (s^{-1}×10^{-3})	Ea (kJ·mol^{-1})
CoMn	0.63	0.62	1.01	201.4
CoMn-0.2 H	1.57	0.80	1.96	162.4
CoMn-10% K	4.01	1.47	2.72	104.2
CoMn-0.2 H-10%K	7.97	2.12	3.76	61.9

anaerobic titration with soot particles as a probe molecule. [24] The TOF_{ov} values (Figs. 5A and S14) were calculated from the isothermal reaction of soot combustion at 300 °C (573 K). It can be seen from Table 3 that CoMn-0.2 H-10%K exhibits the highest TOF_{ov} values (3.76×10^{-3} s^{-1}). The determined activation energy (*Ea*) is presented in Fig. 5B and Table 3. This parameter is instrumental in characterizing the intrinsic activity of the catalysts. Among the catalysts prepared, CoMn-0.2 H-10%K exhibits the lowest *Ea* value at 61.9 kJ·mol^{-1}. This reduced *Ea* value substantially diminishes the energy barrier for the catalytic reaction, facilitating its uninterrupted progression. Consequently, the CoMn-0.2 H-10%K catalyst demonstrates superior intrinsic activity, as evidenced by the outcomes of the isothermal anaerobic reaction and activation energy assessment. Notably, this aligns with its exceptional performance in catalyzing soot combustion.
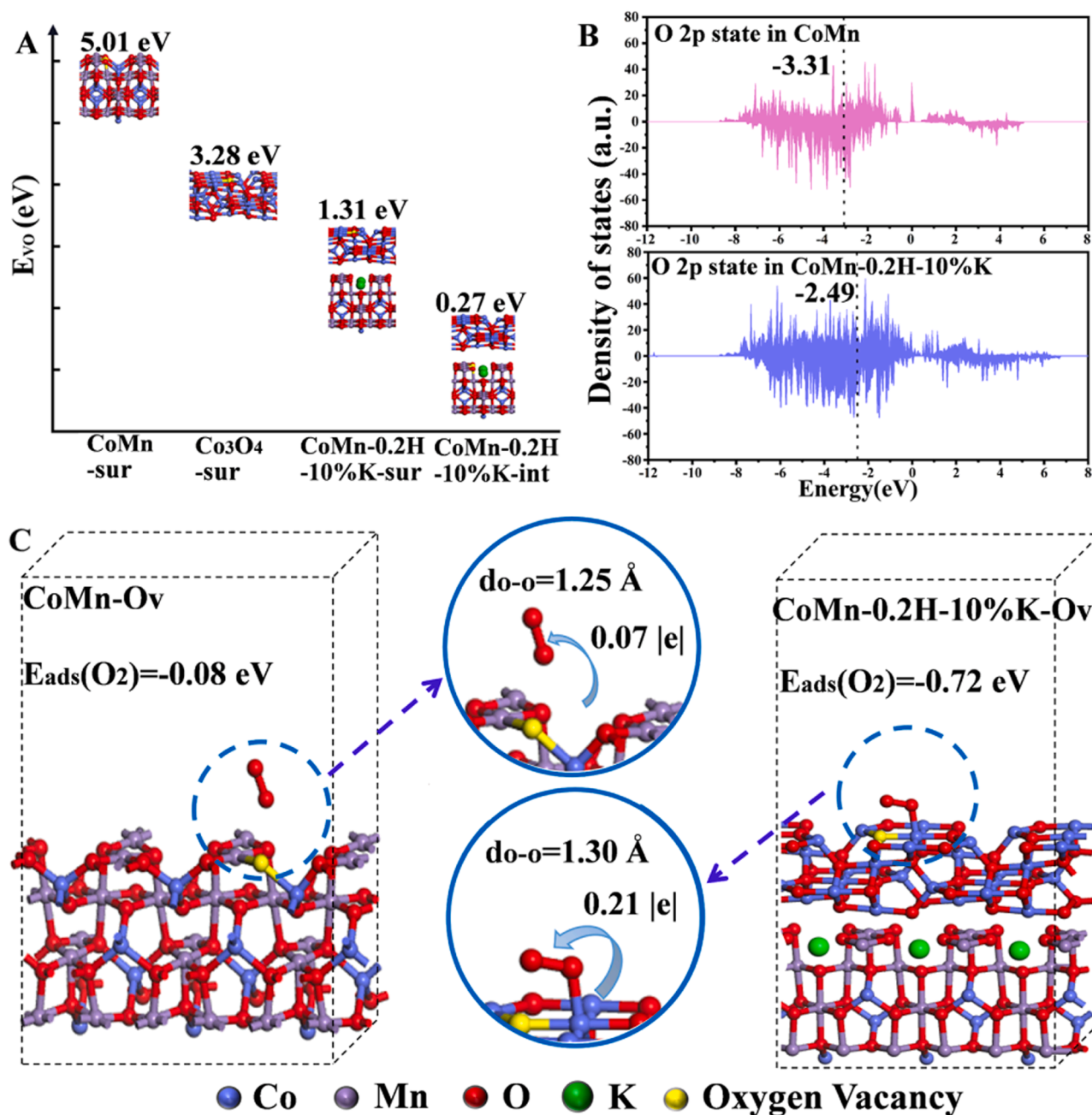
Fig. 6. (A) oxygen vacancy formation energy with different structure (sur: surface; int: interface), (B) calculated projected density of states of the O 2p state for CoMn and CoMn-0.2 H-10%K, (C) structure of CoMn and CoMn-0.2 H-10%K with the presence of oxygen vacancies.

3.3. DFT calculations

DFT calculations were performed to explore the charge transfer in the catalyst and provide a deeper comprehension of the mobility of lattice oxygen species. The (2 2 0) surface of Co_3O_4 with the most TEM exposure was selected as the surface studied in this work and the most stable (001) surface of $CoMn_2O_4$ was studied in this work (Fig. S15) [12, 65]. Bader charge analysis (Fig. 5C and Table S7) revealed a decline in the electron cloud density surrounding oxygen atoms subsequent to the disruption of the Co-O bond. This phenomenon, in turn, could potentially lead to a weakening of the adjacent Mn-O link [66]. The results showed that the length of the Mn-O bond increased from 1.90 to 1.95 Å, indicating a weakening of the Mn-O bond. From Fig. 6A, it can be seen that the surface oxygen vacancy formation energy (E_{VO}) of the dual spinel structure CoMn-0.2 H-10%K catalyst is lower than that of the

original CoMn spinel and the separate Co_3O_4 spinel structure, respectively. This indicates that the formation of oxygen vacancies on the CoMn-0.2 H-10%K surface is thermodynamically favorable. Interestingly, the E_{VO} at the interface of the dual spinel structure is even lower than the surface E_{VO}, indicating that the formation of active oxygen species at the interface is more favorable than that at the surface. In addition, we studied the PDOS of Co, Mn and O. The valence band centers of Mn 3d, Co 3d, and O 2p are larger and more closely spaced in CoMn-0.2 H-10%K than in CoMn spinel, suggesting an enhancement in electron transport between Mn, Co, and O (Figs. 6B, S16, and Table S8) [67,68].

The oxygen adsorption energy (E_{ads}) on CoMn and CoMn-0.2 H-10% K surfaces is shown in Fig. 6C. The E_{ads} of oxygen on CoMn-0.2 H-10%K (-0.72 eV) is lower than that on CoMn (-0.08 eV). The transfer of more electrons is advantageous to the adsorbate-substrate interaction, so we
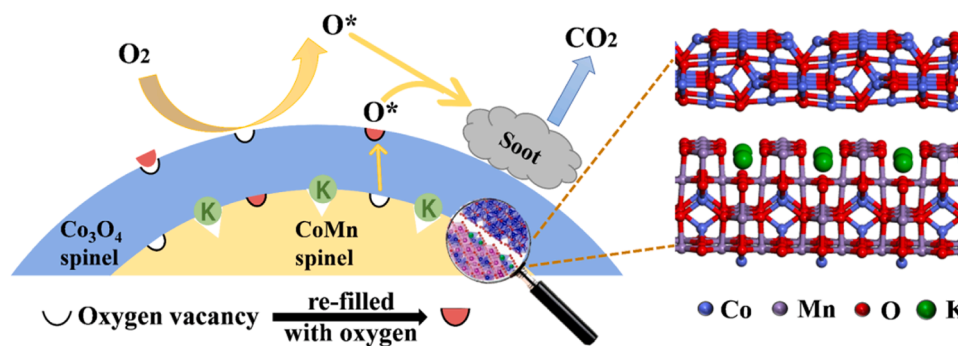
Fig. 7. The schematic diagram of soot oxidation by CoMn-0.2 H-10%K catalyst.

investigated the charge transfer in the adsorption process. Fig. S17 shows the differential charge density before and after the adsorption of oxygen, which implies the existence of an electron transfer process. During oxygen adsorption, it is important to explore the transfer of electrons between the catalyst and the adsorbed oxygen molecules. Fig. 6C illustrates that merely 0.07 $|e|$ is transferred from CoMn spinel to adsorbed O_2, and for CoMn-0.2 H-10%K, 0.23 $|e|$ is transferred to adsorbed O_2. These observations suggest that CoMn-0.2 H-10%K is more likely to activate O_2. Furthermore, the bond lengths after O_2 adsorption were compared. According to the literature [69], the calculated bond length of the O_2 molecule (d_{O-O}) in vacuum is 1.23 Å, supporting the accuracy of our result. Only 0.02 Å of the measured d_{O-O} after CoMn-Ov adsorption is longer than the initial d_{O-O}, showing inadequate O_2 activation. In contrast, the d_{O-O} value of O_2 adsorbed on the CoMn-0.2 H-10%K-Ov surface is 1.30 Å, indicating that O_2 molecules are better activated.

3.4. Catalytic mechanism

The mechanism for soot oxidation over CoMn-0.2 H-10%K was proposed and shown in Fig. 7. During the preparation of the catalyst, the addition of KNO_3 and HNO_3 led to the dissolution of Co and the anchoring of K in the catalyst. After the calcination, more oxygen vacancies would be formed within the catalyst. In addition, K-OMS-2 was found to be formed between the CoMn spinel and the Co_3O_4 spinel. The K-OMS-2 had a high ability for active oxygen generation, which endowed the catalyst with superior performance for catalyst oxidization [13]. Moreover, the lattice distortion at the interface between K-OMS-2 and Co_3O_4 spinel could facilitate the formation of oxygen vacancies and the migration of lattice oxygen species, which was crucial for soot combustion [22,29]. Taken all the above affects, the prepared catalyst of CoMn-0.2 H-10%K had low oxygen vacancy formation energy, a high electron transfer capacity, and an elevated lattice oxygen content. Then a high soot combustion efficiency was obtained for the catalyst.

4. Conclusions

In this work, a series of spinel catalysts were prepared by the self-sacrificing template strategy and used for soot combustion. Among them, the CoMn-0.2 H-10%K catalyst exhibits the best activity with the T_{90} of 365 °C. The CoMn-0.2 H-10%K catalyst was found to have abundant oxygen vacancy and high lattice oxygen mobility. The loading of K in the catalyst could balance the charges of various metals and lead to the formation of K-OMS-2, which has the superior ability to generate active oxygen. The results of DFT calculation further revealed that the CoMn-0.2 H-10%K catalyst has a lower value of E_{VO}, a higher ability of electron transport, and a higher oxygen E_{ads} than the other catalysts. This study provides a potential alternative for noble metal catalysts to eliminate soot at low temperatures, and offers a reference for the rational design and simple preparation of dual spinel structure catalysts.

CRediT authorship contribution statement

Runhan Niu: Writing – original draft, Visualization, Methodology, Investigation, Conceptualization. **Congcong Li:** Visualization, Methodology, Investigation. **Qilong Guo:** Methodology, Investigation. **Panpan Liu:** Project administration. **Changsen Zhang:** Writing – review & editing, Project administration, Methodology, Conceptualization.

Declaration of Competing Interest

The authors declare that they have no known competing financial interests or personal relationships that could have appeared to influence the work reported in this paper.

Data Availability

Data will be made available on request.

Acknowledgements

Appendix A. Supporting information

Supplementary data associated with this article can be found in the online version at doi:10.1016/j.apcatb.2024.124142.

References

[1] H. Yamada, S. Inomata, H. Tanimoto, Mechanisms of increased particle and VOC emissions during DPF active regeneration and practical emissions considering regeneration, Environ. Sci. Technol. *51* (2017) 2914–2923, https://doi.org/10.1021/acs.est.6b05866.
[2] L. Lizarraga, S. Souentie, A. Boreave, C. George, B. D'Anna, P. Vernoux, Effect of diesel oxidation catalysts on the diesel particulate filter regeneration process, Environ. Sci. Technol. *45* (2011) 10591–10597, https://doi.org/10.1021/es2026054.
[3] Z. Shang, M. Sun, S. Chang, X. Che, X. Cao, L. Wang, Y. Guo, W. Zhan, Y. Guo, G. Lu, Activity and stability of Co_3O_4-based catalysts for soot oxidation: the enhanced effect of Bi_2O_3 on activation and transfer of oxygen, Appl. Catal. B: Environ. *209* (2017) 33–44, https://doi.org/10.1016/j.apcatb.2017.02.074.
[4] Y. Wei, Y. Zhang, P. Zhang, J. Xiong, X. Mei, Q. Yu, Z. Zhao, J. Liu, Boosting the removal of diesel soot particles by the optimal exposed crystal facet of CeO_2 in Au/CeO_2 catalysts, Environ. Sci. Technol. *54* (3) (2020) 2002–2011, https://doi.org/10.1021/acs.est.9b07013.
[5] L. Zeng, L. Cui, C. Wang, W. Guo, C. Gong, In-situ modified the surface of Pt-doped perovskite catalyst for soot oxidation, J. Hazard. Mater. *383* (2020), https://doi.org/10.1016/j.jhazmat.2019.121210.
[6] D. Yu, C. Peng, Y. Ren, L. Wang, C. Zhang, X. Fan, X. Yu, Z. Zhao, Low temperature oxidation of diesel soot particles over one-dimensional 2 × 3 tunnel-structured $Na_2Mn_5O_{10}$ catalysts, Appl. Catal. B: Environ. *344* (2024) 123614, https://doi.org/10.1016/j.apcatb.2023.123614.

[7] Y. Di, Y. Xuehua, Z. Chunlei, W. Lanyi, F. Xiaoqiang, Z. Zhen, W. Yuechang, L. Jian, G. Joanna, L. Bartosz, et al., Layered $Na_2Mn_3O_7$ decorated by Cerium as the robust catalysts for efficient low temperature soot combustion, Appl. Catal. B: Environ. *338* (2023) 123022, https://doi.org/10.1016/j.apcatb.2023.123022.

[8] M. Wang, Y. Zhang, Y. Yu, W. Shan, H. He, Synergistic effects of multicomponents produce outstanding soot oxidation activity in a $Cs/Co/MnO_x$ catalyst, Environ. Sci. Technol. *55* (1) (2021) 240–248, https://doi.org/10.1021/acs.est.0c06082.

[9] L. Yan, L. Kai, W. Yuhang, Z. Mingqin, Z. Kun, H. Miaomiao, L. Yun-Quan, Q. Lipeng, C. Bing, Fe-doped Porous Co_3O_4 nanosheets with highly efficient catalytic performance for soot oxidation, Chem. Eng. J. *431* (2021) 133248, https://doi.org/10.1016/j.cej.2021.133248.

[10] Y. Shen, J. Deng, S. Impeng, S. Li, T. Yan, J. Zhang, L. Shi, D. Zhang, Boosting toluene combustion by engineering Co-O strength in cobalt oxide catalysts, Environ. Sci. Technol. *54* (2020) 10342–10350, https://doi.org/10.1021/acs.est.0c02680.

[11] C. Dong, Z. Qu, Y. Qin, Q. Fu, H. Sun, X. Duan, Revealing the highly catalytic performance of spinel $CoMn_2O_4$ for toluene oxidation: involvement and replenishment of oxygen species using in situ designed-TP techniques, ACS Catal. *9* (2019) 6698–6710, https://doi.org/10.1021/acscatal.9b01324.

[12] C. Shan, Y. Zhang, Q. Zhao, K. Fu, Y. Zheng, R. Han, C. Liu, N. Ji, W. Wang, Q. Liu, Acid Etching-induced in situ growth of λ-MnO_2 over CoMn spinel for low-temperature volatile organic compound oxidation, Environ. Sci. Technol. *56* (2022) 10381–10390, https://doi.org/10.1021/acs.est.2c02443.

[13] D. Yu, Y. Ren, X. Yu, X. Fan, L. Wang, R. Wang, Z. Zhao, K. Cheng, Y. Chen, Z. Sojka, et al., Facile synthesis of birnessite-type $K_2Mn_4O_8$ and Cryptomelane-type $K_{2-x}Mn_8O_{16}$ catalysts and their excellent catalytic performance for soot combustion with high resistance to H_2O and SO_2, Appl. Catal. B: Environ. (2020) 119779, https://doi.org/10.1016/j.apcatb.2020.119779.

[14] T. Liu, Q. Li, Y. Xin, Z. Zhang, X. Tang, L. Zheng, P.-X. Gao, Quasi free K cations confined in hollandite-type tunnels for catalytic solid (catalyst)-solid (reactant) oxidation reactions, Appl. Catal. B: Environ. *232* (2018) 108–116, https://doi.org/10.1016/j.apcatb.2018.03.049.

[15] Y. Zheng, Y. Su, C. Pang, L. Yang, C. Song, N. Ji, D. Ma, X. Lu, R. Han, Q. Liu, Interface-enhanced oxygen vacancies of CoCuOx catalysts in situ grown on monolithic Cu foam for VOC catalytic oxidation, Environ. Sci. Technol. *56* (*3*) (2021) 1905–1916, https://doi.org/10.1021/acs.est.1c05855.

[16] L. Yuanwu, H. Lirong, H. René, K. Johannes, Z. Xiaoming, D. Marielle, V. Yana, W. Inez, E. Alexander, D. Marielle, Cobalt-based $Co_3Mo_3N/Co_4N/Co$ metallic heterostructure as a highly active electrocatalyst for alkaline overall water splitting, Angew. Chem. Int. Ed. (2024), https://doi.org/10.1002/anie.202319239.

[17] Y. Yang, W. Si, Y. Peng, Y. Wang, H. Liu, Z. Su, J. Li, Defect engineering on $CuMn_2O_4$ spinel surface: a new path to high-performance oxidation catalysts, Environ. Sci. Technol. *56* (*22*) (2022) 16249–16258, https://doi.org/10.1021/acs.est.2c04858.

[18] B. Sellers-Antón, E. Bailón-García, A. Cardenas-Arenas, A. Davó-Quiñonero, D. Lozano-Castelló, A. Bueno-López, Enhancement of the generation and transfer of active oxygen in Ni/CeO_2 catalysts for soot combustion by controlling the Ni-ceria contact and the three-dimensional structure, Environ. Sci. Technol. *54* (2020) 2439–2447, https://doi.org/10.1021/acs.est.9b07682.

[19] H. Zhao, W. Han, Z. Tang, Tailored design of high–stability $CoMn_{1.5}O_x@TiO_2$ double–wall nanocages derived from prussian blue analogue for catalytic combustion of O–dichlorobenzene, Appl. Catal. B: Environ. *276* (2020) 119133, https://doi.org/10.1016/j.apcatb.2020.119133.

[20] J.-J. Li, E.-Q. Yu, S.-C. Cai, X. Chen, J. Chen, H.-P. Jia, Y.-J. Xu, Noble metal free, $CeO_2/LaMnO_3$ hybrid achieving efficient photo-thermal catalytic decomposition of volatile organic compounds under IR light, Appl. Catal. B: Environ. (2018), https://doi.org/10.1016/j.apcatb.2018.08.069.

[21] W. Linmei, Z. Nanrong, Y. Xinyi, W. Wei, Z. Yi, Z. Zixuan, L. Shanshan, W. Jianli, C. Yaoqiang, Highlights on the key roles of interfaces between CeO_2-based oxide and perovskite ($LaMnO_3/LaFeO_3$) in creating active oxygen species for soot oxidation, Fuel *356* (2023) 129444, https://doi.org/10.1016/j.fuel.2023.129444.

[22] D. Zhu, Y. Huang, R. Li, S. Peng, P. Wang, J.-J. Cao, Constructing active Cu^{2+}–O–Fe^{3+} sites at the CuO–Fe_3O_4 interface to promote activation of surface lattice oxygen, Environ. Sci. Technol. *57* (*45*) (2023) 17598–17609, https://doi.org/10.1021/acs.est.3c05431.

[23] Q. Wang, B. Liu, X. Wang, S. Ran, L. Wang, D. Chen, G. Shen, Morphology evolution of urchin-like $NiCo_2O_4$ nanostructures and their applications as psuedocapacitors and photoelectrochemical cells, J. Mater. Chem. *22* (40) (2012) 21647–21653, https://doi.org/10.1039/c2jm34705a.

[24] P. Zhang, M. Yang, D. Han, X. Liu, X. Yu, J. Xiong, Y. Li, Z. Zhao, J. Liu, Y. Wei, Activating Well-defined α-Fe_2O_3 nanocatalysts by near-surface Mn atom functionality for auto-exhaust soot purification, Appl. Catal. B: Environ. *321* (2023) 122077, https://doi.org/10.1016/j.apcatb.2022.122077.

[25] D. Das, R. Biswas, S. Ghosh, Systematic analysis of structural and magnetic properties of spinel CoB_2O_4(B═Cr,Mn and Fe)compounds from their electronic structures, J. Phys.: Condens. Matter *28* (44) (2016) 446001, https://doi.org/10.1088/0953-8984/28/44/446001.

[26] Z. Hu, X. Zhou, Y. Lu, R. Jv, Y. Liu, N. Li, S. Chen, $CoMn_2O_4$ doped reduced graphene oxide as an effective cathodic electrocatalyst for ORR in microbial fuel cells, Electrochim. Acta *296* (2018) 214–223, https://doi.org/10.1016/j.electacta.2018.11.004.

[27] L. Dr. Sanghan, Y. Gabin, J. Minseul, L. Min-Joon, K. Prof. Kisuk, C. Prof. Jaephil, Hierarchical surface atomic structure of a manganese-based spinel cathode for lithium-ion batteries, Angew. Chem 54 (2014) 1153–1158, https://doi.org/10.1002/ange.201408853.

[28] J.H. Jo, H.J. Kim, N. Yaqoob, K. Ihm, O. Guillon, K.-S. Sohn, N. Lee, P. Kaghazchi, S.-T. Myung, Hollandite-type potassium titanium oxide with exceptionally stable cycling performance as a new cathode material for potassium-ion batteries, Energy Storage Mater. *54* (2023) 680–688, https://doi.org/10.1016/j.ensm.2022.11.015.

[29] Y. Weijie, S. Kailong, W. Jun, M. Yang-Ai, W. Yu, L. Lin, Z. Bicheng, F. Feng, Dual-site oxygen activation for enhanced photocatalytic aerobic oxidation by S-scheme Ni_2P/Bi_3O_4Br-OVs heterojunction, Chem. Eng. J. (2022), https://doi.org/10.1016/j.cej.2022.139425.

[30] M. Zhao, J. Deng, J. Liu, Y. Li, J. Liu, Z. Duan, J. Xiong, Z. Zhao, Y. Wei, W. Song, et al., Roles of surface-active oxygen species on 3DOM cobalt-based spinel catalysts $M_xCo_{3-x}O_4$ (M = Zn and Ni) for NO_x-assisted soot oxidation, ACS Catal. *9* (8) (2019) 7548–7567, https://doi.org/10.1021/acscatal.9b01995.

[31] C. Cao, L. Xing, Y. Yang, Y. Tian, T. Ding, J. Zhang, T. Hu, L. Zheng, X. Li, Diesel soot elimination over potassium-promoted Co_3O_4 nanowires monolithic catalysts under gravitation contact mode, Appl. Catal. B: Environ. *218* (2017) 32–45, https://doi.org/10.1016/j.apcatb.2017.06.035.

[32] Z. Shang, M. Sun, X. Che, W. Wang, L. Wang, X. Cao, W. Zhan, Y. Guo, Y. Guo, G. Lu, The existing states of potassium species in K-doped Co_3O_4 catalysts and their influence on the activities for NO and soot oxidation, Catal. Sci. Technol. *7* (20) (2017) 4710–4719, https://doi.org/10.1039/c7cy01444a.

[33] R. Jimenez, X. Garcia, C. Cellier, P. Ruiz, A. Gordon, Soot combustion with K/MgO as catalyst, Appl. Catal., A *297* (2006) 125–134, https://doi.org/10.1016/j.apcata.2005.08.042.

[34] N. Feng, J. Meng, Y. Wu, C. Chen, L. Wang, L. Gao, H. Wan, G. Guan, KNO_3 supported on three-dimensionally ordered macroporous $La_{0.8}Ce_{0.2}Mn_{1-x}Fe_xO_3$ for soot removal, Catal. Sci. Technol. *6* (9) (2016) 2930–2941, https://doi.org/10.1039/c5cy02025e.

[35] M.E. Gálvez, S. Ascaso, P. Stelmachowski, P. Legutko, A. Kotarba, R. Moliner, M. J. Lázaro, Influence of the surface potassium species in Fe–K/Al_2O_3 catalysts on the soot oxidation activity in the presence of NO_x, Appl. Catal. B: Environ. (2014) 88–98, https://doi.org/10.1016/j.apcatb.2014.01.041.

[36] Z. Peng, F. Nengjie, F. Fan, W. Hui, G. Guofeng, Surface acid etching for efficient anchoring of potassium on 3DOM $La_{0.8}Sr_{0.2}MnO_3$ catalyst: an integration strategy for boosting soot and NO_x simultaneous elimination, J. Hazard. Mater. *409* (2021) 124916, https://doi.org/10.1016/j.jhazmat.2020.124916.

[37] M. Aijing, Z. Yunrong, L. Qiang, W. Xuan, H. Shaopu, L. Dan, T.K. Alex, B. M. Bhekie, G. Jianzhou, Diesel soot oxidation over potassium-promoted urchin-structured NiO-$NiCo_2O_4$ catalyst, Fuel *152* (2023) 118670, https://doi.org/10.1016/j.fuel.2023.128117.

[38] A. Iordan, M.I. Zaki, C. Kappenstein, Interfacial chemistry in the preparation of catalytic potassium-modified aluminas, J. Chem. Soc. Faraday Trans. *89* (1993) 2527–2536, https://doi.org/10.1039/ft9938902527.

[39] Q. Zhao, Z. Yan, C. Chen, J. Chen, Spinels: controlled preparation, oxygen reduction/evolution reaction application, and beyond, Chem. Rev. *117* (15) (2017) 10121–10211, https://doi.org/10.1021/acs.chemrev.7b00051.

[40] C. Rao, J. Shen, F. Wang, H. Peng, X. Xu, H. Zhan, X. Fang, J. Liu, W. Liu, X. Wang, SnO_2 promoted by alkali metal oxides for soot combustion: the effects of surface oxygen mobility and abundance on the activity, Appl. Surf. Sci. *435* (2018) 406–414, https://doi.org/10.1016/j.apsusc.2017.11.109.

[41] R. Yewei, Q. Zhenping, W. Hui, Z. Anlian, Acid-etched spinel $CoMn_2O_4$ with highly active surface lattice oxygen species for significant improvement of catalytic performance of VOCs oxidation, Chem. Eng. J. (2023), https://doi.org/10.1016/j.cej.2023.142316.

[42] G. Fang, C. Zhu, M. Chen, J. Zhou, B. Tang, X. Cao, X. Zheng, A. Pan, S. Liang, Suppressing manganese dissolution in potassium manganate with rich oxygen defects engaged high-energy-density and durable aqueous zinc-ion battery, Adv. Funct. Mater. *29* (2019) 1808375, https://doi.org/10.1002/adfm.201808375.

[43] Y. Shen, J. Deng, X. Hu, X. Chen, H. Yang, D. Cheng, D. Zhang, Expediting toluene combustion by harmonizing the Ce–O strength over Co-doped CeZr oxide catalysts, Environ. Sci. Technol. *57* (2023) 1797–1806, https://doi.org/10.1021/acs.est.2c07853.

[44] Y. Wei, J. Liu, Z. Zhao, Y. Chen, C. Xu, A. Duan, G. Jiang, H. He, Highly active catalysts of gold nanoparticles supported on three-dimensionally ordered macroporous $LaFeO_3$ for soot oxidation, Angew. Chem. (*10*) (2011) 2326–2329, https://doi.org/10.1002/ange.201006014.

[45] Y. Wei, P. Zhang, J. Xiong, Q. Yu, Q. Wu, Z. Zhao, J. Liu, SO_2-tolerant catalytic removal of soot particles over 3D ordered macroporous Al_2O_3-supported binary Pt-Co catalysts, Environ. Sci. Technol. (2020), https://doi.org/10.1021/acs.est.0c00752.

[46] N. Feng, C. Chen, J. Meng, G. Liu, F. Fang, L. Wang, H. Wan, G. Guan, K–Mn supported on three-dimensionally ordered macroporous $La_{0.8}Ce_{0.2}FeO_3$ catalysts for the catalytic combustion of Soot, Appl. Surf. Sci. *399* (2017) 114–122, https://doi.org/10.1016/j.apsusc.2016.12.066.

[47] J. Kaczmarczyk, F. Zasada, J. Janas, P. Indyka, W. Piskorz, A. Kotarba, Z. Sojka, Thermodynamic stability, redox properties, and reactivity of Mn_3O_4, Fe_3O_4, and Co_3O_4 model catalysts for N_2O decomposition: resolving the origins of steady turnover, ACS Catal. *6* (2016) 1235–1246, https://doi.org/10.1021/acscatal.5b02642.

[48] D. Yu, L. Wang, C. Zhang, C. Peng, X. Yu, X. Fan, B. Liu, K. Li, Z. Li, Y. Wei, et al., Alkali metals and cerium-modified La-Co-based perovskite catalysts: facile synthesis, excellent catalytic performance, and reaction mechanisms for soot combustion, ACS Catal. *12* (24) (2022) 15056–15075, https://doi.org/10.1021/acscatal.2c03418.

[49] C. Dong, Z. Qu, Y. Qin, Q. Fu, H. Sun, X. Duan, Revealing the highly catalytic performance of spinel $CoMn_2O_4$ for toluene oxidation: involvement and

replenishment of oxygen species using in situ designed-TP techniques, ACS Catal. (2019), https://doi.org/10.1021/acscatal.9b01324.

[50] H. Liang, B. Jin, M. Li, X. Yuan, J. Wan, W. Liu, X. Wu, S. Liu, Highly reactive and thermally stable Ag/YSZ catalysts with macroporous fiber-like morphology for soot combustion, Appl. Catal. B: Environ. *294* (2021) 120271, https://doi.org/10.1016/j.apcatb.2021.120271.

[51] M. Wang, Y. Zhang, Y. Yu, W. Shan, H. He, Cesium as a dual function promoter in Co/Ce-Sn catalyst for soot oxidation, Appl. Catal. B: Environ. *285* (2020) 119850, https://doi.org/10.1016/j.apcatb.2020.119850.

[52] B. Bassou, N. Guilhaume, K. Lombaert, C. Mirodatos, D. Bianchi, Experimental microkinetic approach of the catalytic oxidation of diesel soot by ceria using temperature-programmed experiments. Part 2: kinetic modeling of the impact of the ceria/soot contacts on the rate of oxidation, Energ. Fuel. *24* (2010) 4766–4780, https://doi.org/10.1021/ef100582w.

[53] L. Jae Hwan, K. Min June, L. Eun Jun, L. Dae-Won, K. Chang Hwan, L. Kwan-Young, Promoting effect of Rh-impregnation on Ag/CeO2 catalyst for soot oxidation, Appl. Surf. Sci. 572 (2021) 151504, https://doi.org/10.1016/j.apsusc.2021.151504.

[54] P. Zhang, J. Xiong, Q. Yu, Y. Li, Y. Wei, Z. Zhao, J. Liu, Efficient purification of auto-exhaust carbon particles over non-noble netals (Fe, Co, Cu) decorated hexagonal NiO nanosheets, FUEL *330* (2022) 125662, https://doi.org/10.1016/j.fuel.2022.125662.

[55] J. Xiong, Q. Wu, X. Mei, J. Liu, Y. Wei, Z. Zhao, D. Wu, J. Li, Fabrication of spinel-type $Pd_xCo_{3-x}O_4$ binary active sites on 3D ordered meso-macroporous Ce-Zr-O2 with enhanced activity for catalytic soot oxidation, ACS Catal. *8* (9) (2018) 7915–7930, https://doi.org/10.1021/acscatal.8b01924.

[56] Y. Wei, P. Zhang, J. Xiong, Q. Yu, Q. Wu, Z. Zhao, J. Liu, SO2-Tolerant CAtalytic Removal of Soot Particles over 3D ordered macroporous Al2O3-supported binary Pt-Co oxide catalysts, Environ. Sci. Technol. *54* (11) (2020) 6947–6956, https://doi.org/10.1021/acs.est.0c00752.

[57] N. Feng, C. Chen, J. Meng, G. Liu, F. Fang, L. Wang, H. Wan, G. Guan, K-Mn supported on three-dimensionally ordered macroporous La0.8Ce0.2FeO3 catalysts for the catalytic combustion of soot, Appl. Surf. Sci. *399* (2017) 114–122, https://doi.org/10.1016/j.apsusc.2016.12.066.

[58] Y.-C. Tsai, H. Nguyen Nhat, J. Lee, Y.-F. Lin, K.-Y.A. Lin, Catalytic soot oxidation using hierarchical cobalt oxide microspheres with various nanostructures: insights into relationships of morphology, property and reactivity, Chem. Eng. J. *395* (2020) 124939, https://doi.org/10.1016/j.cej.2020.124939.

[59] Q. Wu, M. Jing, Y. Wei, Z. Zhao, X. Zhang, J. Xiong, J. Liu, W. Song, J. Li, High-efficient catalysts of core-shell structured Pt@transition metal oxides (TMOs) supported on 3DOM-Al2O3 for soot oxidation: the effect of strong Pt-TMO

[60] D. Jampaiah, V.K. Velisoju, D. Devaiah, M. Singh, E.L.H. Mayes, V.E. Coyle, B. M. Reddy, V. Bansal, S.K. Bhargava, Flower-like Mn3O4/CeO2 microspheres as an efficient catalyst for diesel soot and CO oxidation: synergistic effects for enhanced catalytic performance, Appl. Surf. Sci. *473* (2019) 209–221, https://doi.org/10.1016/j.apsusc.2018.12.048.

[61] W. Ren, T. Ding, Y. Yang, L. Xing, Q. Cheng, D. Zhao, Z. Zhang, Q. Li, J. Zhang, L. Zheng, et al., Identifying oxygen activation/oxidation sites for efficient soot combustion over silver catalysts interacted with nanoflower-like hydrotalcite-derived CoAlO metal oxides, ACS Catal. (2019), https://doi.org/10.1021/acscatal.9b01897.

[62] M. Cortés-Reyes, M.C. Herrera, I.S. Pieta, M.A. Larrubia, L.J. Alemany, In situ TG-MS study of NOx and soot removal over LNT model catalysts, Appl. Catal. A *523* (2016) 193–199, https://doi.org/10.1016/j.apcata.2016.06.004.

[63] Y. Weinan, W. Ya, W. Houlin, Z. Yani, P. Yue, L. Junhua, Water accelerates and directly participates soot oxidation: an isotopic study, Appl. Catal. B: Environ. (2021), https://doi.org/10.1016/j.apcatb.2021.120837.

[64] L. Piotr, F. Monika, G. Joanna, Y. Xuehua, Z. Zhen, A. Andrzej, K. Andrzej, S. Zbigniew, Intricate role of doping with d0 ions (Zr^{4+}, V^{5+}, Mo^{6+}, W^{6+}) on cryptomelane (K-OMS-2) performance in the catalytic soot combustion in presence of NO and SO2, Fuel (2022), https://doi.org/10.1016/j.fuel.2022.125325.

[65] F. Yang, Y. Lu, X. Dong, M. Liu, Z. Li, X. Wang, L. Li, C. Zhu, W. Zhang, C. Yu, et al., Interfacial engineering coupling with tailored oxygen vacancies in Co2Mn2O4 spinel hollow nanofiber for catalytic phenol removal, J. Hazard. Mater. *424* (2022), https://doi.org/10.1016/j.jhazmat.2021.127647.

[66] X.J. Wang, H.Y. Xiao, X.T. Zu, W.J. Weber, A DFT + U Study of Cerium Solubility in La2Zr2O7, J. Nucl. Mater. *424* (2012) 69–74, https://doi.org/10.1016/j.jnucmat.2012.02.008.

[67] T. Wu, S. Sun, J. Song, S. Xi, Y. Du, B. Chen, W.A. Sasangka, H. Liao, C.L. Gan, G. G. Scherer, et al., Iron-facilitated dynamic active-site generation on spinel CoAl2O4 with self-termination of surface reconstruction for water oxidation, Nat. Catal. *2* (9) (2019) 763–772, https://doi.org/10.1038/s41929-019-0325-4.

[68] Y. Chen, Z. Liu, S. Liu, Y. Cheng, C. Zhang, J. Jiao, Y. Lu, W. Wang, K. Sun, X. Bi, et al., In-Situ doping-induced crystal form transition of amorphous Pd-P catalyst for robust electrocatalytic hydrodechlorination, Appl. Catal. B: Environ. *284* (2021), https://doi.org/10.1016/j.apcatb.2020.119713.

[69] R.H. Zhou, P.L. Cao, Molecular cluster-analysis of O2 adsorption and dissociation on Pt(111), Phys. Lett. A *169* (3) (1992) 167–172, https://doi.org/10.1016/0375-9601(92)90587-C.